Karam Zadeh Toularoud, N., Kühn, D., Kriegerowski, M., Lopez Comino, J., Cesca, S., Dahm, T. (2019): Small-aperture array as a tool to monitor fluid injection- and extraction-induced microseismicity: applications and recommendations. - *Acta Geophysica*, *67*, 1, pp. 311—326.

DOI: http://doi.org/10.1007/s11600-018-0231-1

Acta Geophysica manuscript No.
(will be inserted by the editor)

Small aperture array as a tool to monitor fluid injection- and extraction-induced microseismicity: applications and recommendations

Nasim Karamzadeh · Daniela Kühn · Marius Kriegerowski · José Ángel López-Comino · Simone Cesca · Torsten Dahm

Received: DD Month YEAR / Accepted: DD Month YEAR

Abstract The monitoring of microseismicity during temporary, human activities such as fluid injections for hydrofracturing, hydrothermal stimulations or waste water disposal is a difficult task. The seismic stations often cannot be installed on hard rock and at quiet places, noise is strongly increased during the operation itself and the installation of sensors in deep wells is costly and often

N. Karamzadeh,
GFZ German Research Centre for Geosciences and University of Potsdam
Tel.: +49 331 288-1201
Fax: +49 331 288-1204
E-mail: karamzad@gfz-potsdam.de

D. Kühn,
NORSAR, Kjeller, Norway and GFZ German Research Centre for Geosciences

J.A. López-Comino,
King Abdullah University of Science and Technology, huwal, Kingdom of Saudi Arabia and
GFZ German Research Centre for Geosciences

S. Cesca, T. Dahm, M. Kriegerowski and
GFZ German Research Centre for Geosciences

not feasible. The combination of small aperture seismic arrays with shallow borehole sensors offers a solution. We tested this monitoring approach at two different sites, (1) accompanying a fracking experiment in sedimentary shale at 4 km depth, and (2) above a gas field under depletion. The small aperture arrays were planned according to theoretical wavenumber studies combined with simulations considering the local noise conditions. We compared arrays recordings with recordings available from shallow borehole sensors and give examples of detection and location performance. Although the high frequency noise on the 50 m deep borehole sensors was smaller compared to the surface noise before the injection experiment, the signals were highly contaminated during injection by the pumping activities. Therefore, a set of three small aperture arrays at different azimuths was more suited to detect small events, since noise recorded on these arrays is uncorrelated with each other. Further, we developed recommendations for the adaptation of the monitoring concept to other sites experiencing induced seismicity.

Keywords Microseismic monitoring · Induced seismicity · Array seismology · Shallow borehole sensors

1 Introduction

Fluid injection and extraction operations, including those related to hydraulic fracturing, can trigger and induce seismicity through different physical processes, favouring shear failure along pre-existing faults or creating new fractures (Grigoli et al., 2017). Since the first documented cases of earthquakes triggered by fluid injections in the 1970ies (Healy et al., 1968), the number and types of industrial crustal fluid injections or extractions have steadily increased. In recent years, such types of operations were discussed in relation with the occurrence of significant earthquakes, which may lead to damage or change the seismic hazard with a possible feedback to the planning and development of injection projects. Examples include the geothermal stimulation activities in deep hot dry rock environments (Grigoli et al., 2018; Deichmann and Giardini, 2009; Brodsky and Lajoie, 2013), the development of gas storage facilities (Cesca et al., 2014), waste water injections (Ellsworth, 2018; Tadokoro et al., 2000; Horton, 2012; Rubinstein et al., 2014; Hincks et al., 2018), or hydraulic fracturing operation in shale gas (Kim, 2013; Sasaki, 1998).

As a reaction, authorities in different countries have started to define regulations, which often specify criteria for the performance of a monitoring network and the magnitude of completeness. The aim is to be able to detect and locate micro-earthquakes before, during and after injection operations, in order to better understand changes in the seismic hazard and to develop traffic light systems for mitigating the consequences of induced seismicity (e.g. Green et al., 2012).

Monitoring of injection-induced micro-earthquakes in sedimentary basins is challenging due to high background noise level. Detections and locations of such microseismic events are key to judge the effectiveness of geomechanical operations, track the migration of the fracturing processes and ensure the preservation of reservoirs and the integrity of wells. A monitoring system should allow to detect, locate and characterize (1) microseismicity ($Mw < 0.5$) taking place in the vicinity (max 500 m distance) of the operational well, and (2) weak to moderate seismicity ($Mw > 0.5$) taking place at least up to 10 km distance from the operational well. The Mw 0.5 magnitude threshold, as the distance threshold, is indicative and chosen upon our current experience and guidelines of several European states. Specific accuracy in the detection and location of weak events down to a specific minimum magnitude threshold may be needed to track the migration of the fracturing processes, e.g. to ensure the preservation of local underground water reservoirs and the integrity of wells. Similarly, the monitoring should be tuned to allow the prompt detection and characterization of moderate events at further distances, if specific seismogenic faults are recognized in the local surrounding of the operation site.

Often the signal to noise ratios (SNR) are poor, the urban and industrial activities are ongoing during the operations, and the sites may be subject to logistical and environmental restrictions. A seismic monitoring network therefore needs to be not only sufficiently sensitive to detect smallest earthquakes at depth, but also flexible in order to adapt to changing conditions and activities at the surface. Borehole seismometers located in deep monitoring wells reaching basement rocks are usually of high sensitivity and improved SNR. However, they are expensive and cannot be adapted to changing conditions. Seismic monitoring approaches employing a network of shallow boreholes may be an alternative, although the SNR improvement from shallow borehole stations is potentially not very large if the sensors are placed in unconsolidated quaternary layers. A combined network of shallow borehole sensors and small aperture arrays of surface sensors can be interesting, since such installations improve the SNR by stacking and at the same time allow to apply beamforming filter techniques to detect waves with specific slowness.

Small aperture arrays have been used in seismology for a variety of applications, ranging from pure detection arrays for regional seismicity and the study of earthquake swarms associated with natural fluid migration (Hiemer et al., 2012) to studies of induced seismicity in relation to fracking experiments (e.g., López-Comino et al., 2017).

In the present paper, we show and discuss examples of small aperture high frequency arrays combined with shallow borehole sensors to monitor induced seismicity during industrial operations. The array characteristics and transfer functions are discussed in the context of micro-earthquake detection at depth. Field tests have been performed above a gas field under production in the Netherlands and during hydraulic fracturing operations at a depth of about 4 km in Poland. We evaluate the fidelity and SNR of the arrays in comparison to shallow borehole sensors under field conditions. A waveform attribute stacking and beamforming method is applied to detect and partially locate events. We test the arrays' event detection capability by beamforming and compare instances of noise levels between array and shallow borehole stations at different depth levels. In addition, we compare the location ability of one array to network based locations and discussed the benefit of using multiple arrays for event location. Concluding, we provide recommendations on the design of microseismic monitoring networks involving seismological surface arrays.

2 Data

We employ data recorded at a hydraulic fracturing operation in Wysin (Poland), where a seismic monitoring system was installed consisting of surface broadband stations, small-scale arrays and shallow borehole stations. Additionally, we analyse data recorded on a small-aperture seismic array deployed temporarily in Wittewierum above the Groningen gas field (The Netherlands). Both installations were part of the SHEER project (SHale gas Exploration and Exploitation induced Risks, www.sheerproject.eu). In the following, we describe the instrumentation at both sites in more detail.

2.1 The Wysin seismic monitoring system

A dedicated seismic network was installed at a shale gas play close to the village of Wysin in the central-western part of the Peribaltic syncline at Pomerania (Poland). In this area, a Polish oil and gas company drilled two horizontal boreholes designed for fracturing for prospecting and exploration of oil and natural gas. Hydrofracking operations were performed along two horizontal wells at 3955 m and 3865 m depth with an approximate horizontal length of 1.7 km each, in the time periods 9-18 June and 20-29 July, 2016 (López-Comino et al., 2017, 2018).

A hybrid installation, including a distributed network of six broadband stations, three borehole geophones and three small-scale arrays (Fig. 1a) to account for both triggered and induced seismicity in the vicinity of the operational wells, was installed in summer 2015 and fully operational from November 2015 until January 2017. All stations operated in continuous mode. The six broadband stations surround the drilling site at distances between 2.1 and 4.3 km with a good azimuthal coverage (maximal gap 90°). Broadband stations were equipped with GÜRALP CMG-3ESP sensors recording with a sampling rate of 200 Hz. In addition, short-period stations were arranged in three small-scale arrays with apertures between 450 and 950 m. Short period stations were equipped with MARK L-4C-3D sensors (GLOD array) and GeoSIG VE-53-BB sensors (CHRW and PLAC arrays) with sampling rates of 500 Hz. The shallow underground installation is composed of three seismometers installed at 50 m depth (initially Geotech Instruments KS-2000). Seismometers at two borehole stations (GW3 and GW4) were replaced by Nanometrics Trillium Compact Posthole 120s sensors at the end of April 2016 due to technical problems. The sampling rate of all downhole instruments was 500 Hz.

2.2 The Wittewierum array

The objective of the temporary array deployed above the Groningen gas field was to test the usage of a conventional array layout for detection of micro-seismicity. The region of the Groningen gas field is an excellent test ground, since the operating company NAM (Nederlandse Aardolie Maatschappij) installed a multitude of shallow borehole stations from 2014 to 2017, of which 65, in addition to the already existing shallow borehole stations installed by KNMI (Koninklijk Nederlands Meteorologisch Instituut), were already online during the time of measurement, thus ensuring an earthquake catalogue that is complete down to M_L 0.5 during the time of array installation (Dost et al., 2017).

The site for the installation was agreed on with local parties involved in the seismicity monitoring, i.e. KNMI and NAM. Stations were installed from July 12 to August 29, 2016 for a period of almost 50 days. Fig. 1b displays the location of the Groningen gas field with the placement of the array stations shown as blue triangles, and the locations of borehole stations in the vicinity of the array displayed as red circles.

IMS (International Monitoring System) modern small aperture arrays usually consist of a central station plus further stations placed on concentric rings, each with an odd number of sites, spaced at log-periodic intervals (Schweitzer et al., 2012). We based the geometry of the Wittewierum array on this construction, but were not entirely free in choosing the ring diameters and station sites. The array was composed of 9 seismometers and constructed as three concentric rings of 75 m, 150 m and 225 m radius including a central station. Each station consisted of a broadband sensor (Trillium 120 s), an acquisition system (CUBE datalogger), a battery and a GPS antenna. Sensors were installed at about 1 m depth. All array stations recorded continuously with little outages (Cesca et al., 2016).

During the installation time, KNMI registered 18 events, which are listed in Table 1. (`https://data.knmi.nl/datasets/aardbevingen_catalogus/1`), the largest of which had a local magnitude of 1.7 and occurred on July 18, 2016, at a distance of about 11 km to the array. The event closest to the array occurred at a distance of about 5.5 km on July 26, 2016, and had a local magnitude of 0.9.

3 Methodology

3.1 Array assessment

Arrays have a special ability to distinguish between signals with different wavenumbers (slownesses) crossing the array simultaneously. Array signal processing methods are based on improving the SNR by highlighting the arriving seismic waves with a specific wavenumber (slowness) and suppressing the background signals travelling with different wavenumbers (slownesses). The theoretical value of SNR improvement by an array with n stations, is $\sqrt{n}$ (Schweitzer et al., 2012, Eq. 9.7). While the number of array stations controls the SNR gain achievable by the array, the array geometry defines the limits for the resolvable wavenumbers. For instance, small aperture arrays can not distinguish between waves with small wavenumber differences, and for crossing waves with long horizontal wavelengths (λ) compared to the array aperture

(a), such arrays act like a single station. So theoretically, the upper limit for the longest horizontal wavelength that can meaningfully be analysed by array techniques is about the aperture of the array: $\lambda_{max} \simeq a$, so the lower band of resolvable wavenumber, K_{min}, or array resolution is equal to $\frac{2\pi}{a}$. In addition, a wave crossing the array should be sampled by at least two stations, i.e. the smallest recordable wavelength is $\lambda_{min} = 2d_{min}$ assuming d_{min} is the minimum interstation distance, and thus, the maximum resolvable wavenumber is $K_{max} = \frac{\pi}{d_{min}}$.

The array transfer function (ATF) is a standard tool to quantitatively analyse the array performance and to study the capability of the array as seismic monitoring system. The ATF depends on the relative position of array stations and the frequency content of the signals of interest and, for a specific frequency ω, is defined as:

$$\left| \frac{1}{n} \Sigma_{j=1}^{n} e^{i(\mathbf{K}-\mathbf{K_0}).\mathbf{r}_j} \right|^2, \tag{1}$$

where $\mathbf{K} = [k_x, k_y] = \omega[s_x, s_y]$ is the horizontal wavenumber vector, $\mathbf{r}_j = (\delta x_j, \delta y_j)$ is the horizontal location vector of the jth station relative to the array reference point and n is the number of stations (Rost and Thomas, 2002).

The characteristics of the array transfer function such as the presence of side lobes and the shape and sharpness of the main lobe are related to the array layout. For instance, a circular shape of the main lobe implies a symmetric distribution of the array stations ensuring a similar resolution of signals arriving from different backazimuth angles. The width of the main lobe depends on the aperture of the array and defines the array resolution, K_{min}. The larger the aperture of the array, the sharper the main lope and higher the resolution of the array.

The presence and distribution of side lobes depends mainly on the interstation distances and the frequency of the incoming signals. The larger the interstation distances, the closer the side lobes are to the main lobe, which threatens the accurate slowness (wavenumber) determination by increasing the danger of slowness (wavenumber) aliasing depending on the relative beampower ratio between main and side lobes.

The estimation of K_{min} and K_{max} are theoretically valid if the array geometry is regular with uniform interstation distances. Nevertheless, given a potential irregular geometry in the two spatial directions, the true resolution is azimuth dependent (Zywicki, 1999). Experience from ambient vibration studies with synthetic and ground truth data show that the resolution capability of an array lies approximately between $K_{min}/2$ and K_{max} (Wathelet et al., 2008). Additionally, considering the energy content of the signal, even under the best experimental conditions and inside the resolution limits, if the wave energy is too low, identifying the correct wavenumber is difficult and maxima are hardly visible in the slowness-azimuth plane. In practice, the level of incoherent noise rather than the array geometry is the main factor controlling this lower bound (Poggi and Fäh, 2010).

3.2 Array beamforming and event detection

The array beam trace is calculated as the sum of all recorded, time shifted traces:

$$B(t) = \frac{1}{n}\Sigma_j^n \; Y_j(t + dT_j) \qquad \text{with} \qquad dT_j = s_x \delta x_j + s_y \delta y_j. \tag{2}$$

where, Y_j is the trace recorded at the array station j, and n is the number of stations. Assuming the plane wave approximation is valid, the time shift, dT_j, for station j depends on the horizontal slowness components of the incoming wavefront, s_x and s_y, and the relative distance to the array reference point, δx_j and δy_j. The common strategies to find horizontal slowness vector components by estimating the correct values of time shifts and computing the array beam are described in e.g. Schweitzer et al. (2012) and Rost and Thomas (2002).

In the present study, we apply *Lassie*, a recently developed automated full waveform event detection algorithm based on systematic shifting and stacking of smooth characteristic functions and subsequent identification of instances of high coherence in signals recorded at different stations (Lassie, `https://gitext.gfz-potsdam.de/heimann/lassie`; Matos et al., 2018, Heimann et al., in preparation). *Lassie* was initially developed to be applied to data recorded on monitoring networks. We extended *Lassie* using a standard delay-and-sum beamforming approach to shift characteristic functions on a predefined slowness and backazimuth grid. The characteristic functions of traces implement bandpass filtering, taking the absolute, Hanning window convolution, downsampling and final continuous normalization (in that order) to produce a smooth representation of energy contained in the signal. Thanks to efficient implementation and parallelization, the algorithm applies a dense grid search to full waveforms and produces event detections at occurrences of coherent energy crossing the array along with estimates of backazimuth and apparent horizontal slownesses. These information can be employed for signal classification and subsequent event location (Schweitzer et al., 2012).

4 Application

We investigate the theoretical capabilities of the three installed arrays at the Wysin site in Poland (PLAC, GLOD, and CHRW) and at the Wittewierum site above the Groningen gas field in the Netherlands (WARN) with respect to their ability to detect expected target events.

The transfer functions of the arrays are plotted in Fig. 2. In this figure, white arrows displayed in (a)-(c) indicate the direction to expected target events, considering the location of the array and the fracturing experiment (Fig. 1). Red circles show the array resolution (K_{min}). Due to the irregular shape of the arrays at the Wysin site, the array resolutions are not uniform for all backazimuth directions. In contrast, the WARN array's stations are regularly spaced and thus, it is expected to have uniform azimuthal resolution.

Theoretical frequency-wavenumber curves of P- and S-phases resulting from target events are depicted in Fig. 3 providing information on the capabilities of the arrays in terms of resolution and expected aliasing features. The depths of events are assumed to be 4 km and 3 km for the Wysin and Wittewierum area, respectively. The distance dependent wavenumber lines are estimated using the theoretical slowness values depicted in Fig. 4. The distance range in each case is selected according to the expected event distances. The velocity models for two the sites are shown in Fig. 3. In practice, waves may travel with higher slowness values. Especially for the Groningen field, the seismic velocities in the uppermost layers derived recently (Hofman et al., 2017; Kruiver et al., 2017) are much lower than defined in the velocity model depicted in Fig. 3, which was derived from the average velocity model employed by KNMI for event location in the Northern parts of the Netherlands including, but not being limited to the Groningen field (Spetzler and Dost, 2017). For the computation of slownesses, it was combined with the CRUST2.0 model (Bassin, 2000) for depths larger than reservoir depth, since the velocity structure of the deeper part of the Carboniferous layer is not well known (Dost et al., 2017). In addition, S-wave velocities for the sediments down to 3000 m depth were estimated from P-wave velocities using Castagna's relation (Castagna et al., 1985).

In Fig. 3, the value of K_{min} for individual arrays is indicated by the horizontal lines in order to ease discussion and comparison of the expected performance of the three arrays for different frequency content of P- and S- phases for events at different locations in the fracturing zone. The value of the K_{max} for the WARN array is also depicted. For the other arrays, K_{max} is larger than wavenumber range plotted in the figures and therefore is stated only in the figure caption.

4.1 Assessment of the arrays installed at Wysin

In the following, the assessment of the theoretical capability of individual arrays is described in detail:

PLAC: The PLAC array is expected to record events from a distance range of about 2 - 5 km, from the direction shown in Fig. 2a. The ATF of this array shows relatively strong side lobes at about 25 rad/km distance from the main lobe, with relative power as high as 50% of the main lobe. However, these side lobes are not oriented in the expected direction of incoming events and thus, may not cause a problem in estimation of the slowness vector.

Due to the small aperture of this array, the array is not expected to be sensitive to wavenumbers below $K_{min} = 14$ rad/km. According to the Fig. 3, this limiting value of the wavenumber is related to P- and S-phases with certain frequencies and slownesses. Since the slowness in the distance range of 2 - 5 km is increasing with distance (see Fig. 4), the minimum wavenumber is related to the higher frequencies at closer distances and shifts towards the lower frequencies by increasing the epicentral distances. In other words, events at closer distances ($\leq$ 2 - 3 km) with frequency content of P-phases of less than 15 - 20 Hz are not detectable by the array, while for the S-phases, the frequency limits shift towards the lower frequencies (since the slowness of S-phases is higher than that of P-phases), so the related lower frequency bands shift from 7 to 12 Hz for distances 5 to 2 km.

Considering this frequency limitation, P-phases will be difficult to detect in array beams and more likely, events at all distances will be detected once the S-phase energy is exceeding the noise level. The difference in wavenumbers from waves arriving from the edges of the fracturing zone, i.e., at 2 km to 5 km distance, is a fraction of the resolution limit at lower frequencies and is the same as at higher frequencies, which implies that distinguishing events that arrive simultaneously at the array will probably not be possible. The value of K_{max} is about to 62 rad/km, and frequencies up to about 30 Hz are expected to be resolved safely by this array.

GLOD: The GLOD array is situated at a distance of 2 - 3.5 km of the hydrofracturing experiment. According to the ATF shown in Fig. 2b, a secondary lobe is situated in direction of the backazimuth of interest, which is about 20 rad/km away from the main lobe, with the relative power as high as 50% of the main lobe. The wavenumber limit K_{min} for this array is 11.3 rad/km.

So the frequency limit for this array is shifted to lower frequencies compared to the PLAC array. This means that P-phases originating from events at distances of 2 km to 3.5 km with frequencies less than 14 to 16 Hz cannot be detected by the array, while for S-phases, the frequency limit is 6 to 9 Hz. The side lobes at 20 rad/km imposes another limitation on the resolvable signals, since they are situated in the backazimuth range of expected signals. If they lead to spatial aliasing depends on the relative power between main lobe and side lobes. Accordingly, the highest frequency for arriving phases should be considered above which such spatial aliasing would occur, which is 20 Hz and 10 Hz, respectively, for P- and S-phases emanating at distances of 3.5 km.

CHRW: The fracturing operation occurs about 3 to 4 km away from the CHRW array. The ATF of this array is depicted in the Fig. 2c. Although a number of side lobes are present, the expected azimuth direction does not contain any high amplitude secondary lobe. However, some small amplitude side lobes (30% of main lobe amplitude) are visible in those directions. The width of the main lobe is smaller compared to the other arrays as the aperture of the array is larger, allowing this array to be sensitive to lower wavenumbers. The resolution is not uniform in all backazimuth directions, as the array itself is elongated in approximately SW-NE direction. Thus, in this direction, K_{min} is lowest corresponding to the best resolution for small wavenumber differences. Contrary, the resolution is poorest in the SE-NW direction. Therefore, events from the western edge of the hydrofrack will be easier to observe than from the eastern edge. According to Fig. 3, P- and S-phases will be detectable at frequencies above 7 Hz and 2.5 Hz, respectively, at about 4 km epicentral distance. Compared to the other arrays, CHRW array has a better chance to detect P- and S-phase arrivals, however, similar to the other arrays, the resolution of the array to separate between simultaneously arriving waves is insufficient.

4.2 Assessment of the arrays installed at Wittewierum (WARN)

The source-array distance is expected to be about 5 to 20 km and the array is supposed to detect seismic waves originating from all directions.
According to Fig. 2d, the width of main lobe is circular, so the resolution is uniform for all directions. In addition, some relatively strong secondary lobes exist, but only at 40 rad/km from the main lobe. So the array is capable to resolve larger wavenumber ranges.
The array aperture is 0.4 km, which means that K_{min} is about 16 rad/km. According to Fig. 4, for the distance range of 5 to 20 km, P- and S-waves possess constant slowness values of 0.2 and 0.35 s/km for the velocity model assumed for this region, so the frequency limits are not distance-dependent. According to Fig. 3b, the lower frequency limits for P- and S-phases are about 12 Hz and 7 Hz, respectively. In contrast to the arrays installed in Wysin, WARN exhibits an upper frequency limit for P-waves for the epicentral distances of interest at about 22 Hz.

5 Results

5.1 Event detection on the Wysin arrays

We applied the modified version of *Lassie* using a frequency pass band between 9 and 20 Hz. Backazimuths were scanned between -30° to +30° in 0.5° steps and slownesses between 0.05 s/km and 0.3 s/km in 0.01 s/km steps. After manual revision of the detections, we could verify that none of them were of seismic origin from the nearby fracturing site. Most of the detections correspond to local noise sources (López-Comino et al., 2018). An example of waveforms and a detection at array GLOD is depicted in Fig. 5.

5.2 Event detection on the Wittewierum array

In order to process data recorded on the Wittewierum array, we applied a bandpass filter between 9 and 30 Hz following a spectrogram analysis and employed a full backazimuth grid search (from 0° to 360° with a grid step of 5°). Slownesses were scanned between 0 s/km and 0.5 s/km (corresponding to horizontal apparent velocities from 2 km/s to infinity). At first, the detection algorithm was tested on eleven events from the KNMI catalogue that where visible by eye (See column 8 in Table 1) in the data in order to evaluate the detection threshold. Subsequently, the complete data set was processed. An example detection is shown in Fig. 6 for an event that occurred on July 18, 2016 (08:58:11h). The waveforms of this event recorded on the WARN array as well as the KNMI shallow borehole station G28 are depicted in Fig. 7.

The application to the complete data set results in more than 65 000 detections, albeit half of which with a detector strength lower than 16.5. When plotting backazimuth estimates versus slowness for different detector strengths (Fig. 8), there is neither a preferred slowness range nor orientation recognizable. Since seismic events at Groningen are supposed to originate at reservoir depth (Dost et al., 2017), differences in slowness mainly imply changes in the distance to the events. However, with the exception of some events detected with zero slowness, the backazimuth-slowness pattern is similar for all detector strengths, which strengthens the assumption that at least a part of the detections constitutes real events. Detection performance is stable over time, but decreases in the period from the August 20 to August 22, when two stations were malfunctioning.

In addition, *Lassie* detects all events which served for parameter tuning, as well as two additional events catalogued by KNMI that are less obvious in the single seismic traces (See column 9 in Table 1). However, two of those thirteen events exhibit a large difference in backazimuth compared to the KNMI event location (Events number 8 and 15 in Table 1 which are marked by grey stars in Fig. 8). Five other events listed by KNMI where not detected. In general, for the KNMI catalogue events, detection levels correlate with event magnitude and anti-correlate with distance.

The apparent velocities vary between 2 and 6.6 km/s and thus are slightly more variable than what is expected from 1-D raytracing (2.8 km/s to 5 km/s, Fig. 4). In fact, the average velocity model for the Northern Netherlands used to derive slownesses is not describing the complex structure of the Groningen gas field very well. The Rotliegend gas reservoir (average P-wave velocity v_P=3.8 km/s) is overlain by anhydrite with a much higher velocity of v_P=5.9 km/s and underlain by the Carboniferous with v_P=4.25 km/s (Willacy et al., 2018). These high-impedance contrasts channel earthquake energy within the reservoir and result in significant mode conversions (Willacy et al., 2018). In addition, there are strong impedance contrasts between the Zechstein reservoir seal and the overburden as well as within the overburden itself, further complicating the propagation of seismic waves, such that seismograms recorded at the surface contain considerable P-to-S and S-to-P conversions (Willacy et al., 2018). Including single and multiple reflections seismograms are difficult to interpret (Willacy et al., 2018) and beamforming may stack converted instead of direct arrivals due to a wrong phase association. In addition, as mentioned above, seismic velocities, especially S-wave velocities, in the uppermost layers derived recently (Hofman et al., 2017; Kruiver et al., 2017) are much lower than defined in the average velocity model.

It is difficult to distinguish automatically between noise and earthquake signals. One indication is the distribution of events with time of day (Fig. 9). Clearly, the detection distribution with time of day is not even. Additionally, the temporal behaviour varies for different detector strengths; events with a detector strength below 16 occur more often between 21:00 (9:00 P.M.) and 4:00 A.M., whereas events with a detector strength above 18 have a pronounced peak between 21:00 (9:00 P.M.) and 10:30 P.M. and a second between 13:30 and 14:30 (1:30 P.M. and 2:30 P.M.). Most of the detections occur during night time, indicating that the day time noise from superficial sources increases the magnitude of completeness.

Surprisingly, the distribution of events with time seems to be relatively independent of apparent velocity, although the absolute number of detections with apparent velocity lower than 5 km/s is ten times higher than the number of events with apparent velocity between 5 and 10 km/s. That means that a low apparent velocity cannot be used to distinguish between shallow artificial sources close to the array and natural sources at larger distances and depths.

5.3 Event location capability of a single array

In order to locate events using a single array, it would be necessary to form separate beams for P- and S-wave onsets searching different slowness ranges and being filtered in different frequency bands, ensure that direct arrivals are detected and associate phases belonging to the same event prior to locating it based on S-P travel time differences and backazimuth estimate (Mykkeltveit and Bungum, 1984). However, the event location precision of single small aperture arrays is limited due to scatter in the backazimuth and uncertainties in automatically measuring the travel time differences (Schweitzer et al., 2012), such that at seismological observatories, observations from several small aperture arrays as installed at the Wysin site are usually interpreted jointly, employing for example the generalized beamforming location algorithm (Ringdal and Kværna, 1989). Recently, techniques have been developed to integrate array recordings with network recordings for event location (Sick and Joswig, 2016; López-Comino et al., 2017). In addition, the use of multiple use for event location has been picked up (Stipčević et al., 2017).

In the following, we evaluate the location capability of the WARN array. We use a phase detection module developed in-house, which will be integrated into *Lassie* in near future. This module performs a semblance analysis in short moving time windows to measure backazimuths and slowness of arrivals with higher precision than feasible during the *Lassie* automatic beamforming. While events are detected automatically applying a Short Time Average over

Long Time Average (STA/LTA) detector on the semblance traces, accurate $P-$ and $S-$ phases are picked manually based on slowness values. We analyzed time segments of data containing the KNMI reported events. In case of event detection (See the last column in Table 1), the event location is estimated using the S-P arrival time difference as well as the estimated backazimuth employing the velocity model presented in Fig. 3b. The obtained twelve event locations are compared to the KNMI catalogue event locations in Fig. 10. For almost all events, backazimuth estimates agree very well with the KNMI catalogue event locations. The mean deviation is 3°, while the largest is only 11°, whereas the average backazimuth deviation for the detected events using *Lassie* automatic beamforming is 38°, excluding two very large values. The mean value of epicentral mislocation is 2.1 km, whereas its maximum is 5.3 km. However, the error is largest for events closest to the array. Therefore, we suspect that this deviation does not originate from errors in arrival time measurements of P- and S-phases, which would presumably be more randomly distributed, but is caused more likely by an erroneous V_p/V_s ratio. Hofman et al. (2017) demonstrate that especially the shallow S-wave velocities vary significantly, which leads to a laterally fluctuating V_p/V_s ratio. There is no reason to assume that such lateral variations cannot be present in the deeper sedimentary layers as well, which could explain the systematic distribution of error in distance. Such errors in event location can be avoided by employing multiple arrays. Nevertheless, we think that this comparison shows the inherent capability of arrays to measure slowness vectors of incoming waves with high precision.

6 Discussion

In this section. we discuss the special ability of a surface array to reduce the background noise level during fluid injection and extraction experiments. Since at both sites, arrays were operating as a complementary element to surface or borehole sensor installations, we can compare noise levels of surface arrays with nearby borehole instruments.

At the Wysin site, the noise levels at the borehole GW4 and the nearest array, GLOD, both of them in about 2 km distance to the injection well (see Fig. 1), are compared using spectral analysis. Fig. 11 shows the variation of the noise spectral content measured on the starting day of the injection (June 9, 2016) at the array (Fig. 11a) and the borehole (Fig. 11b). The spectral content of the recorded signal at the borehole shows an increase in the two-hour interval between 17:10h and 19:10h (indicated by a blue line on each panel), which is in the agreement with the injection time, whereas at the surface array, such a correlation is not visible. The source of the noise was most likely related to the pumping activity at the surface close to the injection well (López-Comino et al., 2018). More information about the timing of the injection activity is given by (López-Comino et al., 2017).

Fig. 12 shows the noise power spectral density (PSD) during three periods before, during and after fluid injection for the surface array and the borehole station. Ten-minute time windows were analysed and the start time of each period is indicated by white stars on Fig. 11. For the array stations, the PSD is calculated from the array beam, which is formed to detect P-waves generated at the location of the injection at a depth of 4 km. According to the graphs, while the borehole station shows an increase of noise level during the fluid injection for frequencies above 4 Hz, after the injection, the noise level falls to almost the same level as before the experiment, with 10 db fluctuation. However, for frequencies above 60 Hz, the noise is still slightly increased. On the contrary, the noise levels of the array beam before and during the experiment are almost identical, except for the narrow frequency band between 10 Hz to 18 Hz, where the noise level increases about 5 db during the injection. Furthermore, comparing the surface array and borehole analysis, it is concluded that below 6 Hz, the noise level at the surface array is lower than at the borehole station and this pattern is visible for all three periods. However, for frequencies above 6 Hz before the injection, the noise at the array is larger than in the borehole. During the injection experiment, the noise level for frequencies above 60 Hz in the borehole reaches the noise level of the surface

array. Seismic noise at the surface array shows a strong variation before and after hydraulic fracturing, in contrast to borehole stations, where the variation is not significant. This observation can be explained with the higher sensitivity of surface installations to daily variation of human activity producing higher seismic noise during daytime and lower seismic noise during night hours.
Fig. 12b shows the noise level comparison between the WARN surface array at Wittewierum and at different depth levels of the close-by KNMI station G28. This station consists of an accelerometer placed at the surface and 4.5 Hz geophones placed at depths of 50, 100, 150 and 200 m. The horizontal distance between both locations is about 1 km (Fig. 1). The time segments employed for this comparison are 10 minutes long and are extracted before the detection of the largest event with magnitude Ml 1.7 on July 18, 2016. According to the figure, the noise level of the array beam is in general smaller than the noise at a single surface station (see blue dotted and dashed curves). The noise level reduction from a surface measurement (accelerometer) to the 50 m deep instrument (velocity meter) can reach 10 to 15 db in the 3-20 Hz frequency band. By means of array beam forming we can achieve a 5 to 10 db reduction in the noise level for all frequency bands. At frequencies below 3 Hz, the noise level of the array is similar to the noise level on the borehole stations at 200 m depth. For the frequency range of 6-20 Hz, the array beam shows a lower noise level than achieved at 50 m depth in the borehole and the same level as reached at 100 m depth in the borehole. As expected, the high frequency noise on the borehole sensors decreases the deeper the sensors are placed. Below 50 Hz, the incremental decrease with depth is larger the higher the frequencies are. However, the borehole sensor at 100 m depth is an exception, since it shows high noise at frequencies above 30 Hz, increasing even to the noise level of the surface stations (measured on the accelerometer of G28 and the central station of the WARN array). The reason is unclear, but may be related to the local geology and potentially, waveguides at depth.

In general, the noise level at the Wysin site is lower than at the Wittewierum site. Especially, an instrument placed at 50 m depth at Wysin experiences lower noise levels than an instrument placed at 200 m depth above the Groningen field. This is a result of a higher level of cultural noise in the Netherlands compared to Poland (Kraft, 2016) and represents another aspect that should be included when planning a monitoring network. Unfortunately, so far the only source of information are up-front test measurements, since no general database for a comparison of noise levels at different locations is available yet.

7 Conclusions

In this paper, we evaluated the performance of small aperture arrays with respect to their ability to detect target events. For the purpose of planning array measurements before injection experiments, we recommend:

1. In order to design a small aperture array for the specific target to monitor weak induced seismicity at shallow depths, the array transfer function should be analysed and different array geometries should be evaluated and compared, specifying the expected source-receiver distances and expected slowness range of incoming P and S waves, the anticipated magnitudes to be monitored and the estimated frequency range and expected horizontal wavenumber ranges. Figs. 1 and 2 give examples for two real case studies.
2. Plots as shown in Fig. 3 and Fig. 4 are helpful to support the planning of the array design. The velocity models and targeted event depths are used to derive slowness ranges, and from the expected frequencies the range of horizontal wavenumbers. The theoretical wavenumber analysis showed that increasing the aperture of the array leads to a decrease in K_{min} and thus, the crossing point with the wavenumber-distance lines is shifted to lower frequencies. This means that a lower frequency band can be included in the beamforming analysis. Especially for monitoring of nearby microseismicity, increasing the aperture has a limitation, though, since the plane wave approximation may be violated if the aperture of the array is in the same order as the source-array distance.

3. Planning a microseismic monitoring array often is subject to restrictions such as land use, accessibility of the stations, and other logistics. The local noise level at individual stations poses constraints as well, since high noise sites should be definitely avoided. Additionally, the source mechanisms of the individual earthquake events can influence the performance of the array. We suggest to apply synthetic simulations and design the array geometry based on an optimization approach considering all seismological and logistical information about the targeted site and sources. An example is provided in the study by Karamzadeh et al. (2018).

From the specific experience we gained by analysing data recorded by small scale arrays at Wysin and Wittewierum, we conclude:

1. Borehole installations should be combined with surface arrays during hydrofracturing operations. Although no injection-induced event occurred at Wysin above the magnitude of completeness of Mw 0.5, we could demonstrate how hydrofracturing operations impact the SNR at shallow boreholes, while small aperture surface arrays, located at larger distances to the injection well, are less affected. For instance, the shallow borehole installations suffered from very high noise related to the pumping activitites during the injection itself. Therefore, combining boreholes close to the injection site with small aperture arrays at larger distances is beneficial to ensure a constant magnitude of completeness over the full period of the experiment.
2. It is preferrable to employ multiple surface array installations as an alternative to a dense network of borehole sensors, especially in areas experiencing high levels of noise. In case of the Groningen gas field, we could detect a multitude of potential events below the magnitude of completeness of the KNMI catalogue and locate events comprised in the catalogue with $Ml > 0.2$. According to the comparison between KNMI network and single array event locations, the WARN array was capable to determine the backazimuth and arrival time differences of P- and S-phases with high pre-

Table 1 KNMI catalogue. See Fig 10 to compare the locations with the locations obtained from single array beamforming (BF).

No	Date	Time	Lat	Lon	Depth	Ml	Vis. by eye	Event BF	Phase BF
1	2016/07/17	12:01:18.89	53.182	6.887	3	0.5			
2	2016/07/18	08:58:11.50	53.378	6.709	3	1.7	x	x	x
3	2016/07/22	10:55:15.30	53.280	6.855	3	0.3			
4	2016/07/23	17:59:45.00	53.219	6.898	3	0.1			
5	2016/07/26	14:02:10.40	53.277	6.907	3	0.9			
6	2016/07/28	05:32:13.09	53.281	6.860	3	0.2		x	x
7	2016/07/28	15:57:28.10	53.250	6.824	3	0.8	x	x	x
8	2016/08/07	20:40:22.00	53.374	6.644	3	1.3	x	x	x
9	2016/08/08	00:03:39.39	53.170	6.892	3	0.4		x	
10	2016/08/10	18:16:25.30	53.312	6.669	3	0.5	x	x	x
11	2016/08/14	01:50:44.89	53.234	7.019	3	0.7	x	x	x
12	2016/08/14	04:07:50.70	53.220	6.678	3	0.2	x	x	x
13	2016/08/23	02:11:16.10	53.224	7.027	3	0.6			
14	2016/08/23	03:53:30.30	53.223	7.036	3	1.0	x	x	x
15	2016/08/24	13:09:08.40	53.305	6.903	3	0.8	x	x	x
16	2016/08/24	18:44:23.19	53.372	6.724	3	0.6	x	x	x
17	2016/08/24	23:44:03.00	53.354	6.950	3	1.1	x	x	x
18	2016/08/28	03:27:53.10	53.401	6.636	3	1.3	x	x	x

cision. Using more than one array, will decrease the location errors caused by an improper velocity model (Stipčević et al., 2017).

Acknowledgements This work is funded by the EU H2020 SHale gas Exploration and Exploitation induced Risks (SHEER) project (www.sheerproject.eugrant agreement no. 640896). We profoundly thank KNMI (Koninklijk Nederlands Meteorologisch Instituut) for support in installing the instruments of the Wittewierum array as well as KNMI and the Groningen field operator NAM (Nederlandse Aardolie Maatschappij) for identifying a suitable location and obtaining the permissions for installation.

References

Bassin C (2000) The current limits of resolution for surface wave tomography in North America. EOS Trans AGU 81: Fall Meet Suppl, Abstract

Brodsky E, Lajoie L (2013) Anthropogenic seismicity rates and operational parameters at the Salton sea geothermal field. Science 341(6145):543–546, 10.1126/science.1239,213

Castagna J, Batzle M, Eastwood R (1985) Relationships between compressional-wave and shear-wave velocities in clastic silicate rocks. Geophysics 50(4):571–581

Cesca S, Grigoli F, Heimann S, González A, Buforn E, Maghsoudi S, Blanch E, Dahm T (2014) The 2013 September–October seismic sequence offshore Spain: a case of seismicity triggered by gas injection? Geophysical Journal International 198(2):941–953

Cesca S, López-Comino J, Kühn D, Dahm T (2016) Array in wittewierum, netherlands. deutsches geoforschungszentrum gfz. other/seismic network. DOI 10.14470/6P7561560569

Deichmann N, Giardini D (2009) Earthquakes induced by the stimulation of an enhanced geothermal system below Basel (Switzerland). Seismological Research Letters 80(5):784–798, 10.1875/gssrl.80.5.784

Dost B, Ruigrok E, Spetzler J (2017) Development of seismicity and probabilistic hazard assessment for the Groningen gas field. Netherlands Journal of Geosciences 96(5):s235–s245

Ellsworth W (2018) Injection-induced earthquakes. Science 341(6142):10.1126/science.1225,942

Green C, Styles P, Baptie J (2012) Review and recommendations for induced seismicity mitigation. Preese Hall Shale Gas Fracturing - Induced Seismicity Report pp 1–22

Grigoli F, Cesca S, Priolo E, Rinaldi AP, Clinton JF, Stabile TA, Dost B, Fernandez MG, Wiemer S, Dahm T (2017) Current challenges in monitoring, discrimination, and management of induced seismicity related to underground industrial activities: A European perspective. Reviews of Geophysics 55(2):310–340

Grigoli F, Cesca S, Rinaldi A, Malconi A, López-Comino J, Westaway R, Cauzzi C, Dahm T, Wiemer S (2018) The November 2017 Mw 5.5 Pohang earthquake: A possible case of induced seismicity in South Korea. Science p 10.1126/science.aat2010

Healy J, Rubey W, Griggs D, Raleigh C (1968) The Denver earthquakes. Science 161:1301–1310–351

Hiemer S, Rössler D, Scherbaum F (2012) Monitoring the West Bohemian earthquake swarm in 2008/2009 by a temporary small-aperture seismic array. Journal of Seismology 16:169–182, DOI 10.1007/s10950-011-9256-5

Hincks T, Aspinall W, Cooke R, Gernon T (2018) Oklahomas induced seismicity strongly linked to wastewater injection depth. Science 161:10.1126/science.aap7911

Hofman L, Ruigrok E, Dost B, Paulssen H (2017) A shallow seismic velocity model for the Groningen area in the Netherlands. Journal of Geophysical Research: Solid Earth 122(10):8035–8050

Horton (2012) Disposal of hydrofracking waste fluid by injection into subsurface aquifers triggers earthquake swarm in Central Arkansas with potential for damaging earthquake. Seismological Research Letters 83(2):doi.org/10.1785/gssrl.83.2.250

Karamzadeh N, Heimann S, Dahm T, Krüger F (2018) Application based seismological array design by seismicity scenario modelling. Geophysical Journal International 216(3):1711–1727, DOI 10.1093/gji/ggy523

Kim WY (2013) Induced seismicity associated with fluid injections into a deep well in Youngstown, Ohio. Journal of Geophysical Research 118(7):3506–3518

Kraft T (2016) A high-resolution and calibrated model of man-made seismic noise for europe. 76th Annual Meeting of the DGG (German Geophysical Society), 14-17.03.2016, Münster, Germany

Kruiver P, van Dedem E, Romijn R, de Lange G, Korff M, Stafleu J, Gunnink J, Rodriguez-Marek A, Bommer J, van Elk J, Doornhof D (2017) An integrated shear-wave velocity model for the Groningen gas field, The Netherlands. Bulletin of Earthquake Engineering 15(9):3555–3580

López-Comino J, Cesca S, Kriegerowski M, Heimann S, Dahm J T and Mirek, Lasocki S (2017) Monitoring performance using synthetic data for induced microseismicity by hydrofracking at the Wysin site (Poland). Geophysical Journal International 210(1):42–55

López-Comino J, Cesca S, Jarosławski J, Montcoudiol N, Heimann H, Dahm T, Lasocki S, Gunning A, Capuano P, Ellsworth W (2018) Induced seismicity response of hydraulic fracturing: results of a multidisciplinary monitoring at the Wysin site, Poland. Scientific Reports in press:251–267

Matos C, Custódio S, Batló J, Zahradník J, Arroucau P, Silveira G, Heimann S (2018) An active seismic zone in intraplate West Iberia inferred from high-resolution geophysical data. Journal of Geophysical Research: Solid Earth 123(4):2885–2907

Mykkeltveit S, Bungum H (1984) Processing of regional seismic events using data from small-aperture arrays. Bulletin of the Seismological Society of America 74(6):2313–2333

Peterson J (1993) Observations and modeling of seismic background noise. US Geological Survey Albuquerque, New Mexico, Tech rep

Poggi V, Fäh D (2010) Estimating Rayleigh wave particle motion from three-component array analysis of ambient vibrations. Geophysical Journal International 180(1):251–267

Ringdal F, Kværna T (1989) A multi-channel processing approach to real time network detection, phase association, and threshold monitoring. Bulletin of the Seismological Society of America 79(6):1927–1940

Rost S, Thomas C (2002) Array seismology: methods and applications. Rev Geophys 40(3):1008

Rubinstein J, Ellsworth W, McGarr A, Benz H (2014) The 2001-present induced earthquake sequence in the Raton Basin of Northern New Mexico and Southern Colorado. Bulletin of the Seismological Society of America 104(5):10.1785/012,014

Sasaki S (1998) Characteristics of microseismic events induced during hydraulic fracturing experiments at the Hijori hot dry rock geothermal site. Tectonophysics 289:171–188

Schweitzer J, Fyen J, Mykkeltveit S, Gibbons S, Pirli M, Kühn D, Kværna T (2012) New Manual of Seismological Observatory Practice (NMSOP-2), IASPEI, GFZ German Research Centre for Geosciences, chap 9, pp 1–80

Sick B, Joswig M (2016) Combining network and array waveform coherence for automatic location: examples from induced seismicity monitoring. Geophysical Journal International 208(3):1373–1388

Spetzler J, Dost B (2017) Hypocentre estimation of induced earthquakes in Groningen. Geophysical Journal International 209(1):453–465

Stipčević J, Kennett BL, Tkalčić H (2017) Simultaneous use of multiple seismic arrays. Geophysical Journal International 209(2):770–783

Tadokoro K, Ando M, Nishigami K (2000) Induced earthquakes accompanying the water injection experiment at the Nojima fault zone, Japan: seismicity and its migration. Journal of Geophysical Research 105(B3):6089–6104

Wathelet M, Jongmans D, Ohrnberger M, Bonnefoy-Claudet S (2008) Array performances for ambient vibrations on a shallow structure and consequences over V_s inversion. Journal of Seismology 12(1):1–19

Willacy C, van Dedem E, Minisini S, Li J, Blokland J, Das I, Droujinine A (2018) Application of full-waveform event location and moment-tensor inversion for Groningen induced seismicity. The Leading Edge 37(2):92–99

Zywicki DJ (1999) Advanced Signal Processing Methods Applied to Engineering Analysis of Seismic Surface Waves. PhD thesis, Georgia Institute of Technology

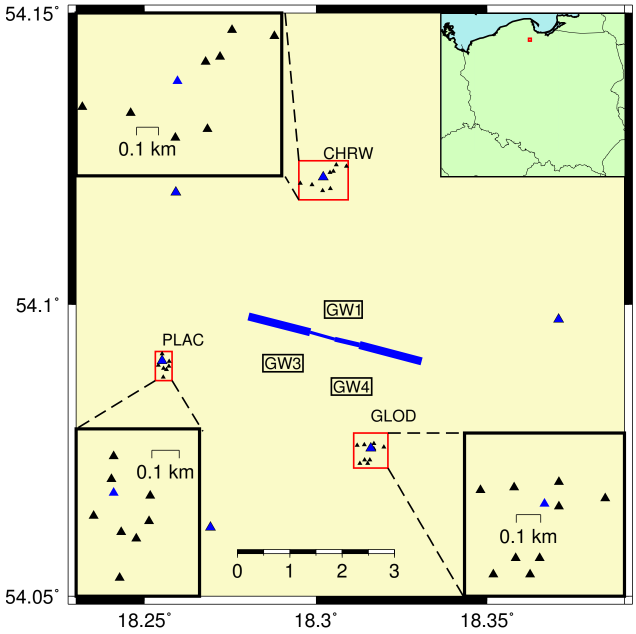

(a)

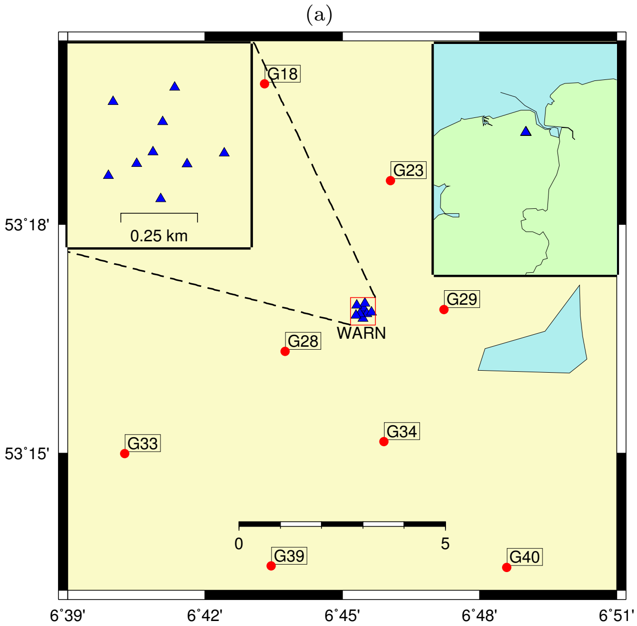

(b)

Fig. 1 a) Overview of the Wysin hydrofracturing experiment site in Poland and the locations of the installed seismic stations to monitor related induced seismicity. b) Wittewierum site above the Groningen gas field, the Netherlands. Blue line in (a) shows the location of the fluid injection at the depth of 4 km. In (a) and (b): red dots show the location of borehole stations. Blue triangles represent broadband stations and black triangles mark short-period stations. Red rectangles show location of inset maps.

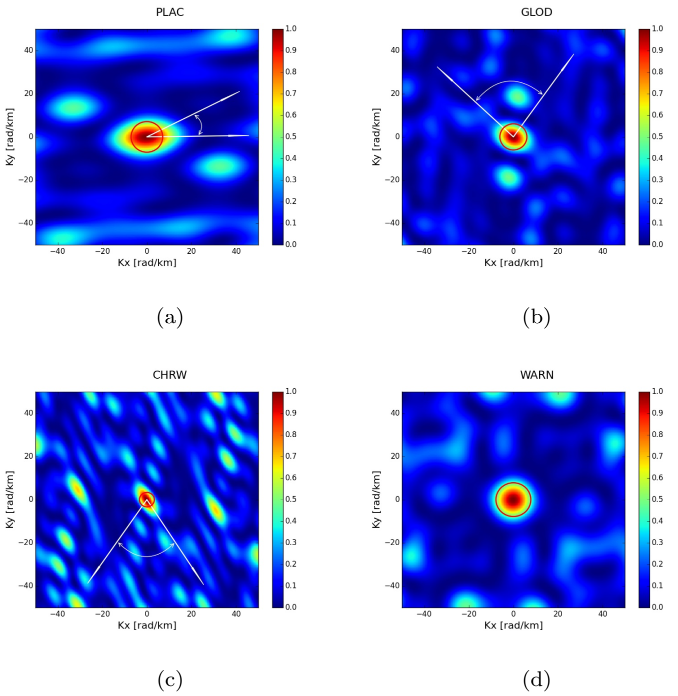

Fig. 2 Array transfer functions (ATFs) for the three arrays at Wysin (a)-(c) and Wittewierum (d). Red circles show the width of the main lobe which is equivalent to the array resolution, i.e. K_{min}. The arrows in (a)-(c) indicate the expected backazimuth range for incoming signals as inferred from Fig. 1.

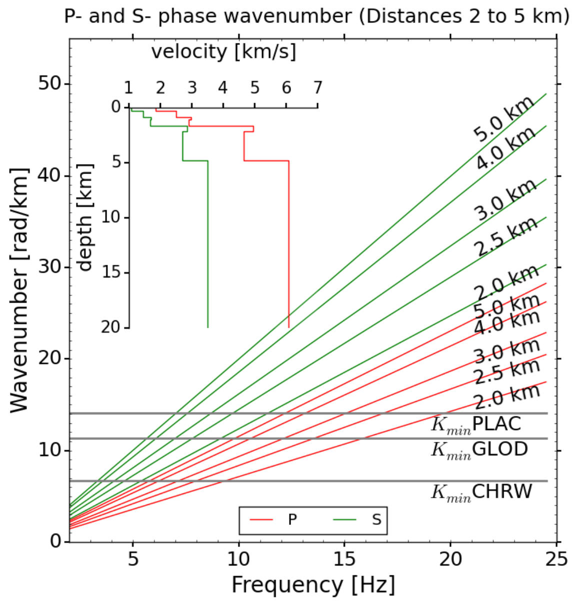

(a)

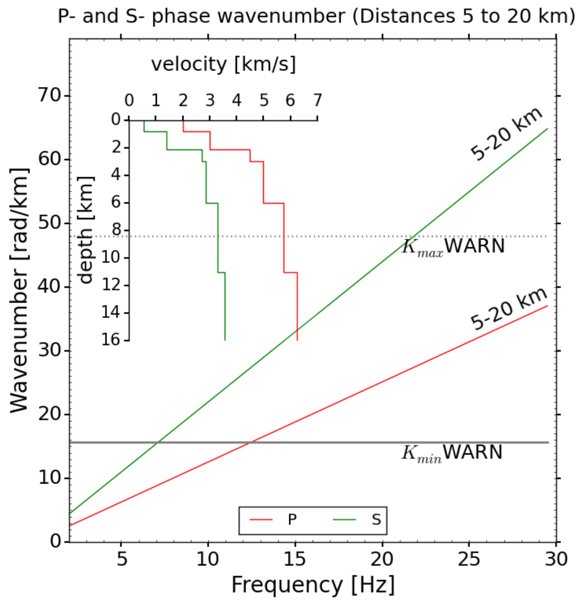

(b)

Fig. 3 Theoretical wavenumbers of P- and S-phases for the frequency range of incoming waves and expected epicentral distances and depths for (a) arrays at the Wysin sites PLAC, GLOD and CHRW and (b) the array at the Wittewierum site (WARN). The velocity models that are used to estimate slownesses are shown, and depths of events are 4 km and 3 km in (a) and (b), respectively. The value of K_{min} is indicated for each array by a horizontal solid black line. The values of K_{max} for the PLAC, CHRW and GLOD arrays are 61, 45 and 52.5 rad/km, respectively. For the WARN array, it is about 48 rad/km, which is indicated in (b) by the horizontal dotted line.

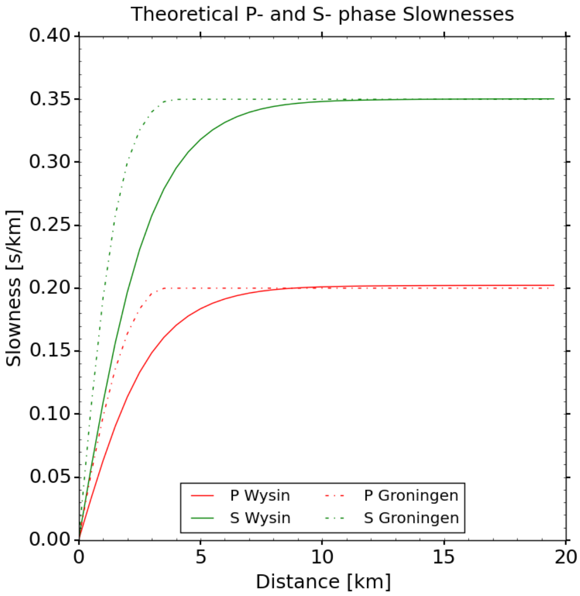

Fig. 4 Theoretical slownesses of P- and S-phases for the Wittewierum (dashed lines) and Wysin (solid lines) arrays for an assumed event at 3 km and 4 km depth respectively; the velocity models are shown in Fig. 3.

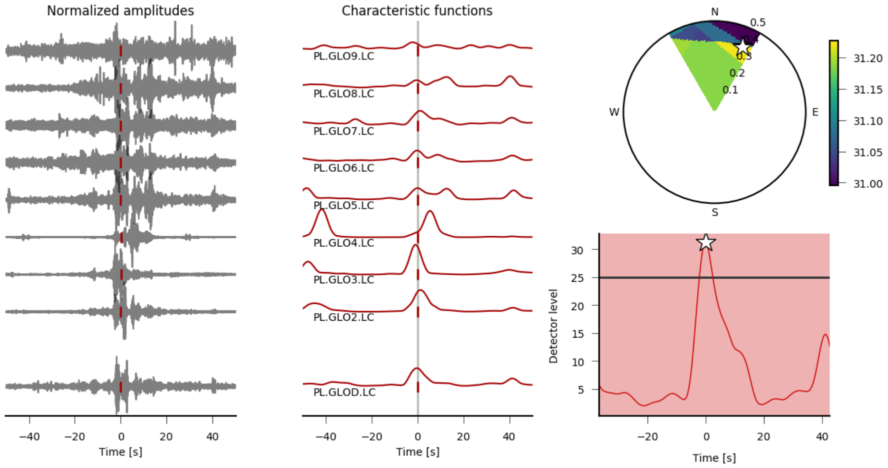

Fig. 5 A detection on the GLOD array shortly after the injection was stopped (see white star no. 1 in Fig. 11). This detection is not confirmed to be an event related to the hydrofracturing experiment. a) Left: filtered seismic traces; centre: characteristic functions, vertical dashes mark applied shifts according to the maximum in the slowness-backazimuth domain; top right: slowness-backazimuth slice coloured by amplitude of stacked characteristic functions, white star denotes the maximum coherence; bottom right: detector level, the white star represents the local maximum detected once the coherence exceeds the detector threshold indicated by the black horizontal line.

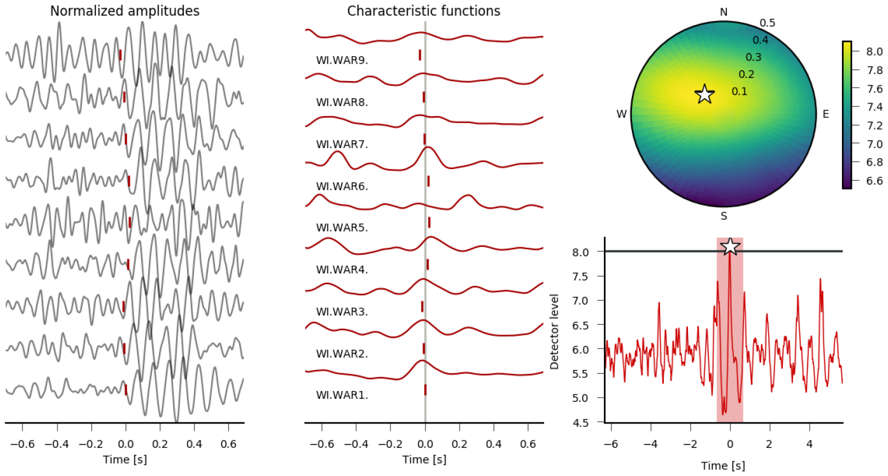

Fig. 6 Example of event detected by *Lassie* on the WARN array on July 18, 2016. For a description of the plot see caption of Fig. 5.

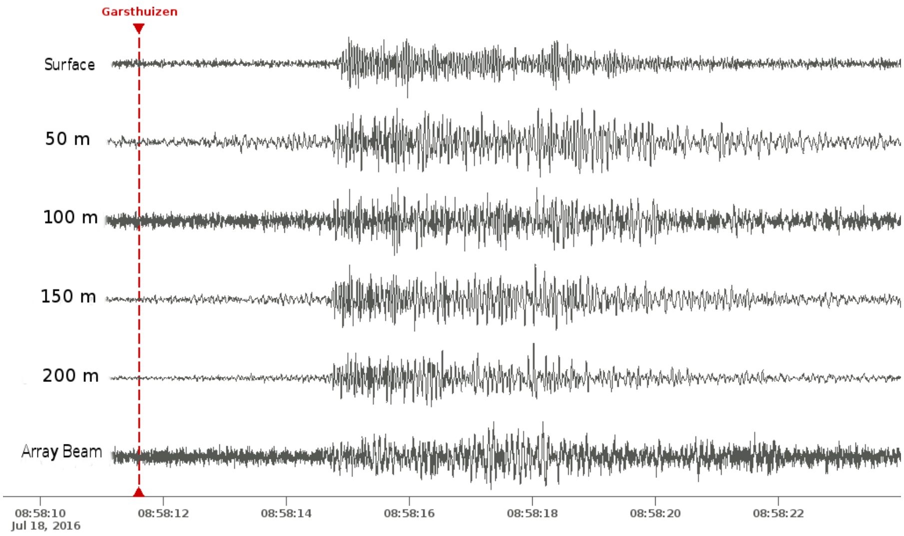

Fig. 7 Waveforms of the event on July 18, 2016 (08:58:11). The five top traces are recorded at the G28 shallow borehole station. The top trace stems from the surface accelerometer, the following four traces from different levels within the borehole. The last trace shows the WARN array's beam (according to the P-phase horizontal slowness vector).

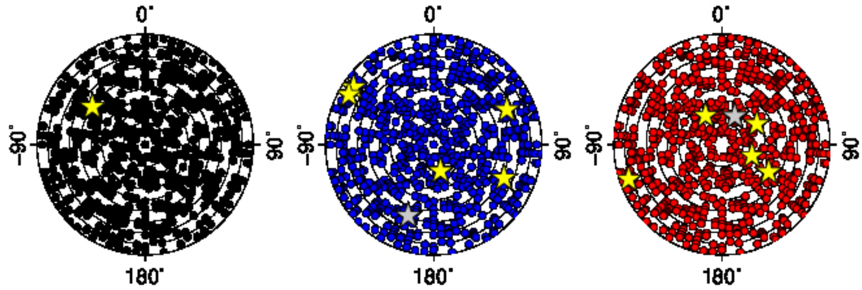

Fig. 8 Polar plots showing the distribution of measured backazimuths and slownesses for different detector strengths (slowness varies from 0 s/km in the centre to 0.5 s/km at the outer rim, intergrid line distances correspond to 0.05 s/km). Left: detector strength < 16.5, middle: detector strength between 16.5 and 18, right: detector strength > 18. Stars indicate events registered in the KNMI catalogue.

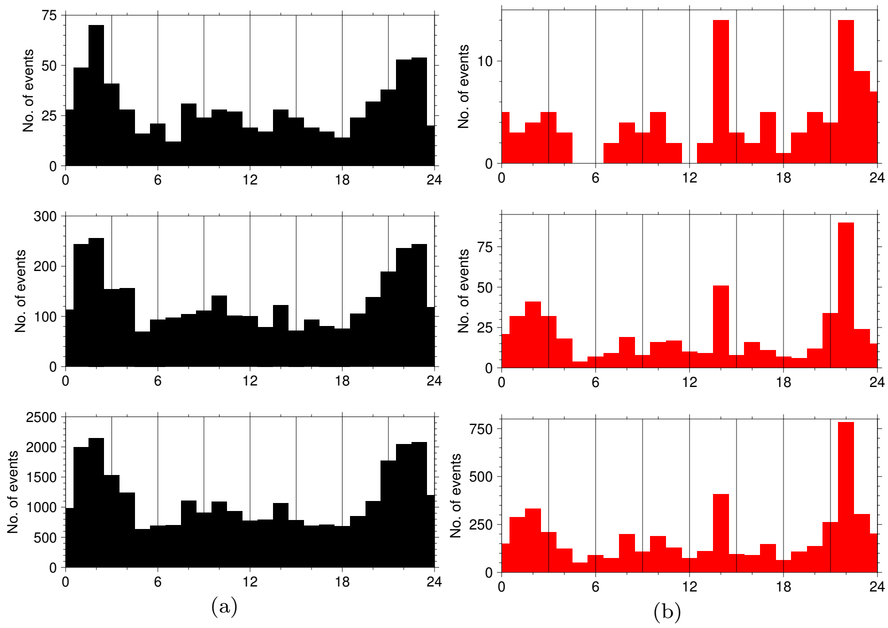

Fig. 9 Distribution of the number of events with time of day for three different ranges of apparent velocity (top: apparent velocity > 10 km/s, middle: apparent velocity between 5 and 10 km/s, bottom: apparent velocity < 5 km/s); left: detector strength < 16, right: detector strength > 18.

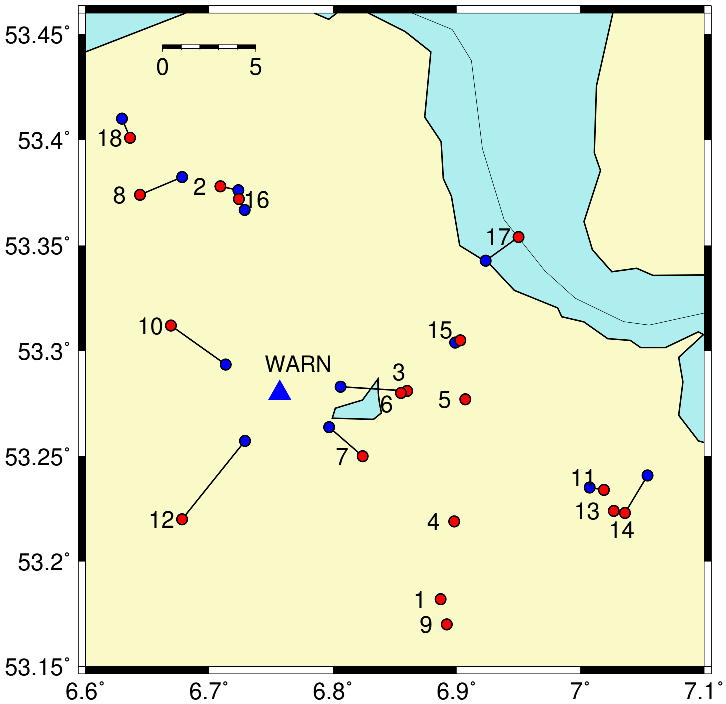

Fig. 10 Blue triangle shows the WARN array. Red circles are locations reported in KNMI catalogue (Table 1) and blue circles are location calculated from single array beamforming method (phase detection module). Numbers are in accordance with the numbers in Table 1.

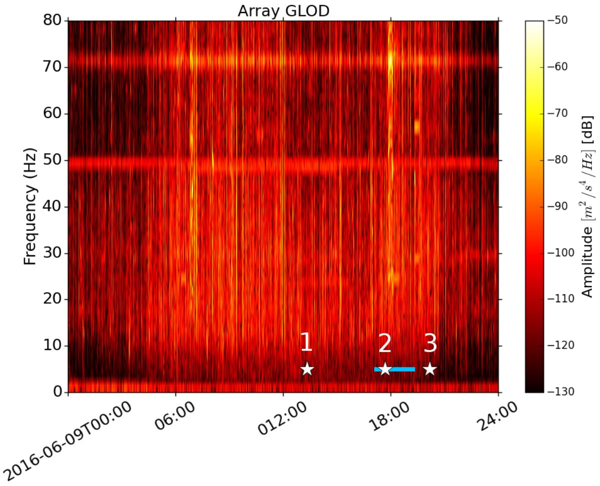

(a)

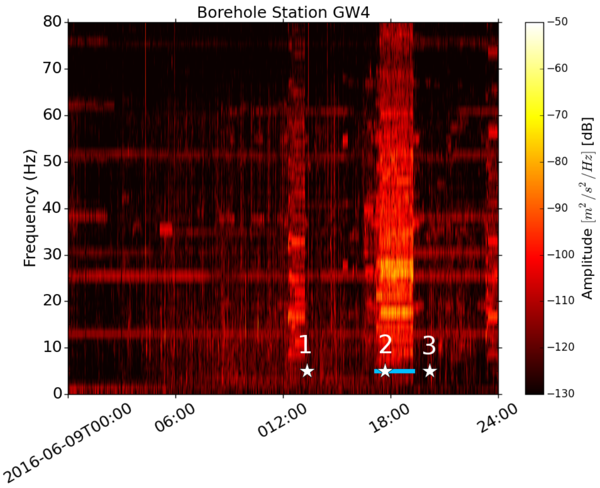

(b)

Fig. 11 Noise spectral variation during the hydrofracturing operation at about 2 km distance from the injection point measured on a) a surface array beam (GLOD) and b) at a borehole station (GW4) (see Fig. 1 for the locations of instruments). The blue lines on each plot show the injection time period and the three white stars show the start time of the two-minute time segments used to compare the PSD (Fig. 12) for three periods before, during and after the injection.

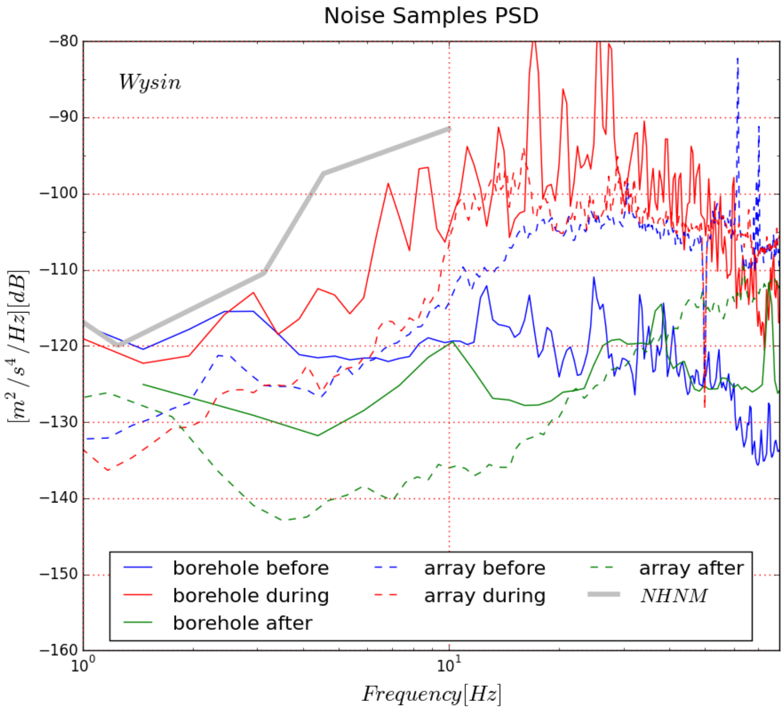

(a)

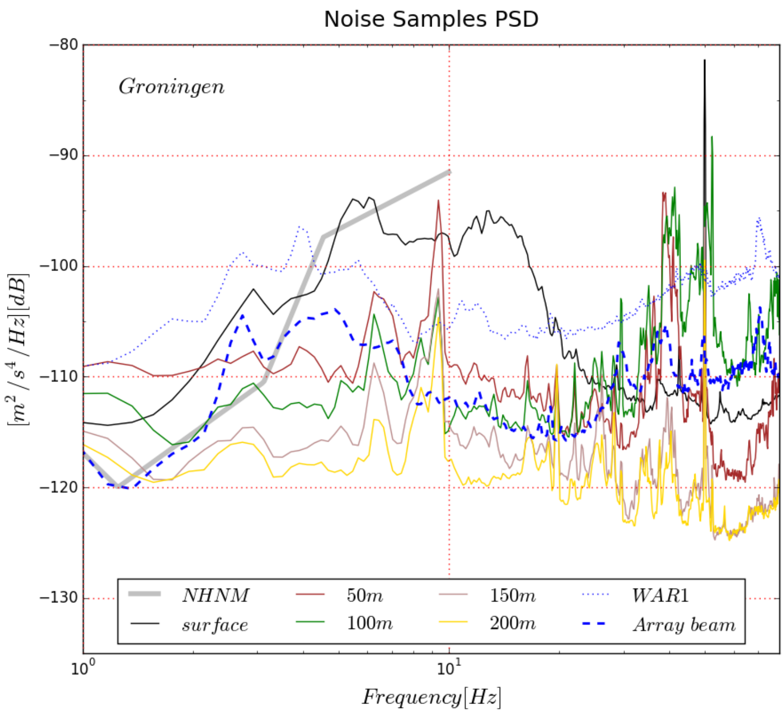

(b)

Fig. 12 PSD of the noise samples recorded during a) three periods before (blue lines), during (red lines) and after (green lines) the hydrofracturing experiment in Wysin and b) in Wittewierum The thick grey line displays the new high noise model according to Peterson (1993). In a), solid lines mark PSDs of recordings in the borehole, wheras dashed lines display PSDs of recordings on the surface array. In b), solid lines mark PSDs of recordings from the instruments of the shallow borehole station G28, the dashed blue line indicates the PSD of the WARN array's beam and the dotted blue line displays the PSD of a record from the central array station, WAR1.